Synthesis and structural, magnetic, electric, and thermoelectric characterization of layered Rh$_{1-x}$Ir$_x$Te$_2$ (0 ⩽ x ⩽ 1)

Florencia E. Lurgo,[1] Fernando Pomiro,[1,2] Raúl E. Carbonio ◉,[1,*] and Rodolfo D. Sánchez ◉[3,†]

[1]*INFIQC (CONICET- UNC), Departamento de Fisicoquímica, Facultad de Ciencias Químicas, Universidad Nacional de Córdoba, Haya de la Torre Esq. Medina Allende, Ciudad Universitaria, X5000HUA Córdoba, Argentina*

[2]*Department of Chemistry, University of Warwick, Gibbet Hill, Coventry CV4 7AL, United Kingdom*

[3]*Instituto de Nanociencia y Nanotecnología (INN), CNEA-CONICET, Centro Atómico Bariloche, Comisión Nacional de Energía Atómica and Instituto Balseiro, Universidad Nacional de Cuyo, Av. Bustillo 9500, (8400) San Carlos de Bariloche (RN), Argentina*

Crystallographic analysis and thermoelectric studies of solid solutions Rh$_{1-x}$Ir$_x$Te$_2$ (0 ⩽ x ⩽ 1) are reported. All compositions show layered structures belonging to the $P\bar{3}m1$ space group at room temperature. IrTe$_2$ presents a first-order phase transition from the hexagonal to the triclinic lattice ($P\bar{1}$ space group), which is monitored by synchrotron radiation x-ray powder diffraction. In the cooling-down process the transition appears at 240 K while in the warming-up process it begins at 280 K, showing a remarkable hysteresis. All compositions show a strong metallic behavior with enhanced Pauli paramagnetism and two regimes in the electrical resistivity. These regimes are associated with electron-electron scattering (at low temperature $\rho \sim T^2$) and electron-phonon coupling (higher temperatures $\rho \sim T$). The Seebeck coefficient shows hole-type carriers for all the compounds.

I. INTRODUCTION

Thermoelectric chalcogenides have been studied in recent years due to their novel electrical properties; however, these new materials are not environmentally friendly for technological applications [1,2]. Bi$_2$Te$_3$ has been the most studied thermoelectric chalcogenide and crystallizes in a layered structure belonging to the $R\bar{3}m$ space group; the layers stacked along the c axis are $\cdots$Te-Bi-Te-Bi-Te$\cdots$ Te-Bi-Te-Bi-Te$\cdots$ with strong covalent bonds in the layer Te-Bi-Te-Bi-Te and weak van der Waals bonds between layers Te-Te. These weak bonds explain the cleavage along the plane perpendicular to the c axis and the anisotropic thermal and electrical transport properties shown in this material [3]. For these reasons we believe that layered chalcogenides are suitable candidates for the development of materials with unique electrical and thermoelectric properties.

In the search for new chalcogenides for technological applications that crystallize in layered structures, the dichalcogenides MX_2 belonging to the structural families CdI$_2$, CdCl$_2$, and MoS$_2$ have shown good thermoelectric properties [4–6]. Their structural analysis has been reported in recent years [7,8]. These compounds show a variety of crystal structures depending on the temperature at which they have been synthesized; for example, AuTe$_2$ crystallizes in two different distortions of the CdI$_2$ structural type: $C2/m$ (calaverite) at 600 °C [6,9] and $Pma2$ (krennerite) at 425 °C [7,10–12]. The metal/Te ratio is also very important in determining the crystal structure of the system, for instance, for the

rhodium-tellurium chalcogenide: (i) Rh/Te = 1.00 crystallizes in $P6_3/mmc$ (NiAs type), (ii) Rh/Te = 1.33 crystallizes in $I2/m$ (Cr$_3$S$_4$-type structure), (iii) RhTe$_x$ crystallizes in $P\bar{3}m1$ (CdI$_2$-type structure) if the ratio is 1.33 < Rh/Te ⩽ 2, (iv) if the ratio is 2 ⩽ Rh/Te ⩽ 2.44 it crystallizes in $Pa\bar{3}$ (pyrite-type structure), and (v) Rh/Te = 2.88 crystallizes in $R\bar{3}m$ [13,14].

IrTe$_2$ shows a structural phase transition at approximately 250 K, where formation of Ir-Ir bonds occurs along the b axis. The breaking of Ir-Ir bonds that occurs in Ir$_{1-x}$Pt$_x$Te$_2$ results in the appearance of a structural critical point in the $T \rightarrow 0$ limit, at $x_c \approx 0.035$. Albeit both IrTe$_2$ and PtTe$_2$ are paramagnetic metals, superconductivity is induced at $T_c = 3.1$ K by the bond breaking in a narrow range of $x \geqslant x_c$ in Ir$_{1-x}$Pt$_x$Te$_2$ [15]. Additionally, IrTe$_2$ is of particular interest as both Ir and Te have high atomic numbers. Spin-orbit coupling is expected to be high which may lead to exotic states such as topological superconductivity [16,17]. Unconventional superconductivity (SC) often emerges in the proximity of symmetry-breaking electronic and magnetic orders upon their destabilization by chemical modifications, external pressure, and fields, as seen in a diverse variety of quantum systems [18–20].

In addition, chalcogenides with two different metal cations, such as Ir$_{1-x}$Pt$_x$Te$_2$, Ir$_{1-x}$Rh$_x$Te$_2$, Mn$_{1-x}$Cr$_x$Se, and Mn$_{1-x}$Ti$_x$Se, show interesting properties such as superconductivity and higher thermoelectric power as the number of charge carriers decreases compared with the dichalcogenides with a single metal cation [21–27].

For the reasons previously mentioned, we decided to synthetize and crystallographically, electrically, and magnetically characterize the family of dichalcogenides Rh$_{1-x}$Ir$_x$Te$_2$ in the whole compositional range, 0 ⩽ x ⩽ 1). The synthesis and

*rcarbonio@unc.edu.ar
†rodolfosanchez@cnea.gob.ar

TABLE I. Synthesis condition of $Rh_{1-x}Ir_xTe_2$. All samples have been synthetized with a temperature ramp of 5 °C/min.

Sample	$RhTe_2$	$Rh_{0.75}Ir_{0.25}Te_2$	$Rh_{0.50}Ir_{0.50}Te_2$	$Rh_{0.25}Ir_{0.75}Te_2$	$IrTe_2$
Thermal Treatment	1200 °C 72 h	1125 °C 60 h 30 min	1050 °C 48 h	975 °C 36 h 30 min	950 °C 6 h + 600 °C 18 h

structural characterization of Rh-rich compounds are developed in this work.

II. EXPERIMENT

Polycrystalline samples of $Rh_{1-x}Ir_xTe_2$ with $x = 0$, 0.25, 0.50, 0.75, and 1 were synthetized using the solid-state method with elemental precursors (Rh, Ir, and Te, high purity, 99.9% Strem Chemicals) in vacuum evacuated quartz ampoules. Table I shows the synthesis conditions to obtain the purest version of each sample. $RhTe_2$ might crystallize in both layered and pyrite structures [28]. We found that a fast cooling down of the sample (quenching with liquid nitrogen) is essential to stabilize the layered metastable phase $P\bar{3}m1$ over the pyrite one. Otherwise, the pyrite phase is always observed after the thermal treatment.

X-ray powder diffraction (XRPD) experiments were performed with a PANalitycal X'Pert Pro diffractometer using Bragg-Brentano geometry to determine the purity of the samples. The structure was crystallographically characterized using synchrotron radiation x-ray powder diffraction (SR XRPD) at the I11 beamline (high resolution powder diffraction) at the Diamond Light Source. Data were collected with two different detectors: a multianalyzer crystal detector (MAC) and a position sensitive detector (PSD). High resolution and low background diffractograms were obtained with MAC detectors and good resolution and high intensity with PSD detectors. Samples were loaded in a borosilicate capillary spinner 0.1 mm in diameter. $RhTe_2$, $Rh_{0.25}Ir_{0.75}Te_2$, and $Rh_{0.50}Ir_{0.50}Te_2$ were measured with PSD detectors at 100 and 300 K. The rest of the compositions were measured with MAC detectors at 100 K and 300 K. For $IrTe_2$ and $Rh_{0.75}Ir_{0.25}Te_2$ experiments were performed on warming and on cooling in the temperature range from 300 to 100 K using the PSD detector and measuring a pattern every 2 K. Data were collected in the 2θ range 2°–90°. The zero-point error, wavelength (≈ 0.826 Å), and instrument contribution to the peak profiles were determined against a NIST 640 Si standard and fixed in all subsequent analyses. The crystal structure refinements were performed by using the Rietveld method [29] with the FULLPROF SUITE program [30]. Scanning electronic microscopy (SEM) images were collected from two different microscopes: field-emission scanning electron microscope (FE SEM) Sigma and SEM FEG (Field Emission Gun) FEI Nova NanoSEM 230. Energy dispersive x-ray spectroscopy (EDAX) measurements were performed on a SEM FEG (Field Emission Gun) FEI.

Magnetization measurements were performed in a commercial MPMS-5S superconducting quantum interference device magnetometer on powdered samples in gelatin capsules from 5 to 300 K at 100 Oe in warming conditions. Also, magnetization in warming and cooling processes at 5000 Oe was measured for $x = 1$ and $x = 0.25$ samples.

The temperature dependence of electric resistivity [$\rho(T)$] and Seebeck effect [$S(T)$] experiments were performed in a multipurpose equipment with two sample holder lances. Pellets of the samples were cut in a rectangular polyhedron prism with approximately $(11 \times 2 \times 2)$mm^3. $\rho(T)$ was measured in the temperature range 5–300 K using a cryostat with liquid helium, while $S(T)$ was measured between 80 and 300 K using a cryostat with liquid nitrogen. To measure the Seebeck effect, two LakeShore 330 temperature controllers and a HP 34420A nanovoltmeter were used. For electrical resistivity measurements a programmable Keithley 6220 DC current source using constant electrical current between 0.1 and 100 mA and the same nanovoltmeter and temperature controller were used.

III. RESULTS AND DISCUSSIONS

A. Crystallographic characterization

1. $Rh_{1-x}Ir_xTe_2$ with $x = 0$, 0.25, 0.50, 0.75 at 100 and 300 K

The SR XRPD data of $Rh_{1-x}Ir_xTe_2$ with $x = 0$, 0.25, 0.50, 0.75 collected at 300 and 100 K were correctly refined using the layered $P\bar{3}m1$ (No. 164) model (see Fig. 1 and Fig. S1 and Table S1 in the Supplemental Material [31]). Table II summarizes the refined unit cell parameters, Te and Rh/Ir occupancies, and reliability factors obtained from SR XRPD data for $Rh_{1-x}Ir_xTe_2$ at 300 K. In the structure with space group $P\bar{3}m1$, Rh^{4+}/Ir^{4+} cations are randomly distributed in the 1a Wyckoff sites (0, 0, 0). All samples showed less than 1.0% w/w precursors impurity except the sample $Rh_{0.75}Ir_{0.25}Te_2$ that presents 4.5% w/w pyrite as impurity.

$Rh_{0.75}Ir_{0.25}Te_2$ was refined using the $P\bar{3}m1$ space group at both temperatures (100 and 300 K). Nevertheless, we observe a change in the Bragg reflections of the hexagonal phase in the temperature range 100–300 K (decreasing intensity), which suggests a phase transition, and this occurs in a large temperature range. In Figs. 2(a)–2(c) the Bragg reflections' evolution of the $P\bar{3}m1$ phase show an intensity decrease suggesting a phase transition; the pyrite phase impurity does not play an important role in this phase transition, since at the measured temperature range, the pyrite phase does not show any change in the intensity of the Bragg reflections. In Figs. 2(d) and 2(e) is shown the thermal evolution (300–100 K) of the most important Bragg reflections of the pyrite phase (18° and 24.5°) and evidence that there is no change in intensity. In future analysis, SR XRPD measurements at lower temperatures ($T < 100$ K) should be performed to elucidate this possible phase transition.

Additionally, Table II shows the refined compositions obtained from the occupancy values (Occ). $Rh_{0.50}Ir_{0.50}Te_2$ and $Rh_{0.25}Ir_{0.75}Te_2$ show Te deficiency but do not show detectable Te impurity peaks in the PXRD patterns. The compound $Rh_{0.75}Ir_{0.25}Te_2$ does not show Te as an impurity and this may
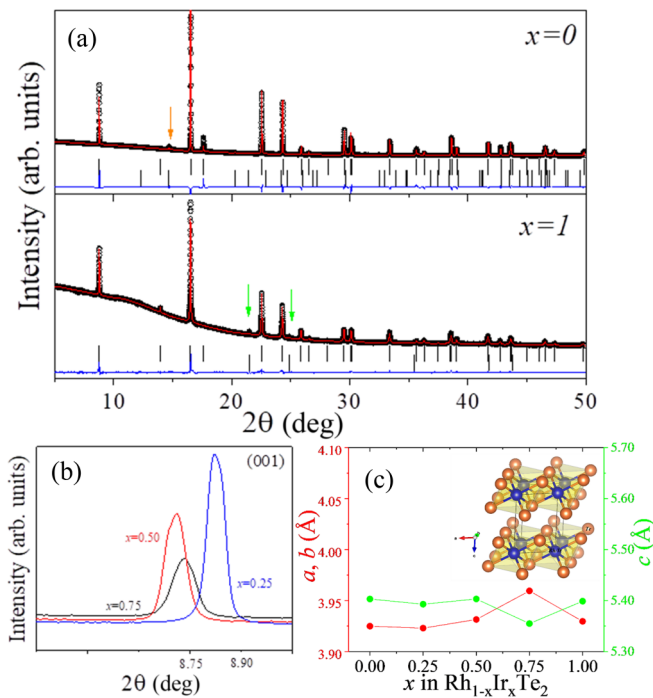
FIG. 1. (a) Refined SR XRPD pattern for the compositions $x = 0$ and $x = 1$ obtained at 300 K. Observed pattern in black dots; calculated pattern in red lines; difference between observed and calculated in blue lines and Bragg reflections in black bars (arrows indicate the most important reflections of impurities Te in $x = 0$ and Ir in $x = 1$). (b) Evolution of the intensity and 2θ of the plane (001) in the compositions with $x = 0.25$, 0.50, and 0.75. (c) Unit cell parameters as a function of Ir substitution in RhTe$_2$. Inset: $P\bar{3}m1$ structure using the VESTA program [32].

be due to the presence of the pyrite phase. The deficiency of Te in this compound can be crystallized in the pyrite phase. This was particularity evidenced in the SEM images and EDAX analysis with Te-rich regions and small bubbles of Te (see Fig. S2 [31]), which allowed us to hypothesize about the synthesis mechanism. Our hypothesis is that Te reacts in the gas phase with the metal precursors in the solid phase. We propose this because we observed an orange/brown gas inside the quartz ampoule a few seconds before quenching it, suggesting that two phases are involved in the synthesis. Additionally, the vaporization temperatures of Te and the metals Rh/Ir are quite different. The T_{vap} of Te is 987.8 °C, which is extremely low compared to the rest of the precursors ($T_{\mathrm{vap}}^{\mathrm{Rh}} = 3.697$ °C and $T_{\mathrm{vap}}^{\mathrm{Ir}} = 4.130$ °C). When we quenched the ampoules, Te gas abruptly condensed, producing the small bubbles of Te observed in SEM images at all compositions (see Fig. S2 in the Supplemental Material [31]).

The lattice parameter a at 300 K slightly increases with Ir content in the compositions $x = 0.25$, 0.50, and 0.75, but IrTe$_2$ shows a lattice parameter very similar to RhTe$_2$. This occurs due to the small increase in ionic radii [$r(\mathrm{Rh}^{4+})$ 0.600 Å and $r(\mathrm{Ir}^{4+})$ 0.625 Å]. The lattice parameter c at 300 K slightly decreases with the Ir content, but the composition $x = 0.75$ shows a significant decrease and this can be attributed to the presence of the pyrite phase. Ir^{4+}/Rh^{4+} ions (M) are octa-

hedrally coordinated by six Te^{2-} ions and the face sharing of MTe$_6$ octahedra forms MTe$_2$ layers. These layers are bonded by Te-Te bonding rather than weak van der Waals forces [33].

The Rh-Te system is extremely complex because the ratio Te/Rh, synthesis method, and thermal treatment determine the obtained structure. Using evacuated quartz ampoules for the synthesis method the hexagonal $P\bar{3}m1$ phase was stabilized in the compositional ratio range $1.33 < \mathrm{Te/Rh} \leqslant 2.00$ [13,28,33]. Ding *et al.* [13] prepared this compound using an isopiestic method, at 900°C for 23 days obtaining the monoclinic $I2/m$ phase in the compositional ratio range $1.09 \leqslant \mathrm{Te/Rh} \leqslant 1.74$ and the hexagonal $P\bar{3}m1$ phase in the compositional ratio range $1.74 < \mathrm{Te/Rh} \leqslant 2.00$. According to the literature, stoichiometric $P\bar{3}m1$ RhTe$_2$ does not exist at room temperature since there is Te segregation during the synthesis. The samples crystallized in $P\bar{3}m1$ with the higher content of Te reported in the literature up to now are Rh$_{1.06}$Te$_2$ (Te/Rh $= 1.88$) and Rh$_{1.16}$Te$_2$ (Te/Rh $= 1.72$) [28]; we obtained the composition Rh$_{1.22}$Te$_2$.

2. Thermal evolution of the crystal structure of IrTe$_2$ in the range 100–300 K

IrTe$_2$ shows a first-order phase transition in the temperature range from 100 to 300 K. Both phases were correctly refined at 300 and 100 K using the $P\bar{3}m1$ and $P\bar{1}$ (No. 2) space groups, respectively (see Fig. 1 and Fig S1 in the Supplemental Material [31]). In Table III are shown the refined unit cell parameters, Te and Ir occupancies (refined compositions), and reliability factors obtained from SR XRPD at 100 K for IrTe$_2$.

Temperature-dependent evolution of the cr lattice parameter in IrTe$_2$ together with the R_{wp} for the refinement performed with a single-phase model ($P\bar{1}$) are summarized in Fig. 3. In this figure we also show a heat map denoting the changes observed in the reflection (0 1 –1) throughout the phase transition. Figure 3 displays a clear discontinuity of the c parameter around the phase transition. Full thermal dependence of the lattice parameters is given in Fig. S3 (see Supplemental Material [31]). The phase transition shows a clear hysteresis; during cooling the transition starts around 250 K while in warming it starts around 275 K, in total agreement with the literature [34].

The origin of the phase transition in IrTe$_2$ has been studied in recent years and there is still controversy around its understanding. Transmission electron microscopy (TEM) experiments and electron diffraction (ED) patterns suggest that the structural transition is due to Ir-Ir and Te-Te dimer formation with a modulation wave vector $\vec{q} = (\frac{1}{5}, 0, -\frac{1}{5})$. This evidence determines that phase transition is produced by a charge-orbital density wave (DW) [34], but ^{125}Te NMR experiments suggested that the transition is due to a lattice distortion at low temperature, and it did not provide any evidence for charge DW order [35]. Additionally, theoretical studies indicated that the transition is caused by crystal field effects, which split the Te energy levels in p_x, p_y, and p_z, resulting in a reduction of the kinetic energy of the electronic system [36].

TABLE II. Refined unit cell parameters, Te and Rh/Ir occupancies, refined compositions, and reliability factors obtained from SR XRPD for $Rh_{1-x}Ir_xTe_2$ at 300 K. Note: Nominal compositions are written in the text.

Compound	$RhTe_2$	$Rh_{0.75}Ir_{0.25}Te_2$	$Rh_{0.50}Ir_{0.50}Te_2$	$Rh_{0.25}Ir_{0.75}Te_2$	$IrTe_2$
Main phase (%w/w)	99	95.5	100	100	98.5
a Å	3.92496(2)	3.92303(2)	3.93148(3)	3.95956(2)	3.92966(2)
b Å	3.92496(2)	3.92303(2)	3.93148(3)	3.95956(2)	3.92966(2)
c Å	5.40313(4)	5.39299(3)	5.40327(7)	5.35495(4)	5.39886(5)
V (Å^3)	72.085(1)	71.879(1)	72.327(2)	72.708(1)	72.201(1)
α (deg)	90	90	90	90	90
β (deg)	90	90	90	90	90
γ (deg)	120	120	120	120	120
Rh $1a$ (0,0,0)					
Occ	0.10196(5)	0.06008(5)	0.04015(5)	0.01988(3)	
Ir $1a$ (0,0,0)					
Occ		0.02315(3)	0.04315(3)	0.06344(4)	0.08317(3)
Te $2d$ (1/3, 2/3, z)					
z	0.74600(1)	0.74522(2)	0.75741(3)	0.74926(2)	0.74765(3)
Occ	0.16667(2)	0.16667(2)	0.13592(4)	0.14908(3)	0.16744(2)
R_p (%)	27	13.1	33	24.8	20.7
R_{wp} (%)	25.4	8.15	22.8	3.48	15.1
R_{expt} (%)	1.62	3.32	4.38	2.7	3.92
R_{Bragg} (%)	12.9	3.52	14.6	12.7	3.78
R_{factor} (%)	5.88	2.46	13.5	14	3.32
Refined compositions	$Rh_{1.22}Te_2$	$Rh_{0.72}Ir_{0.28}Te_2$	$Rh_{0.48}Ir_{0.52}Te_{1.63}$	$Rh_{0.24}Ir_{0.76}Te_{1.80}$	$IrTe_2$
Te/Rh	1.64[a]				

[a]The compositional ratio Te/Rh agrees with the literature [13,28,33].

B. Magnetic behavior

We subtracted the diamagnetic contributions of the capsule and the diamagnetic atomic cores (i.e., for $IrTe_2$ $\chi_{cores} \approx -169 \times 10^{-4} \frac{emu}{mol\ Oe}$) from the magnetic susceptibility (M/H).

In Fig. 4(a) we show the thermal evolution of χ for the series. The tail observed at low T is the Curie paramagnetism $\chi_{Curie} \sim \frac{1}{T}$ associated with localized spins, presumably due to some magnetic impurity which is quite common in dichalco-
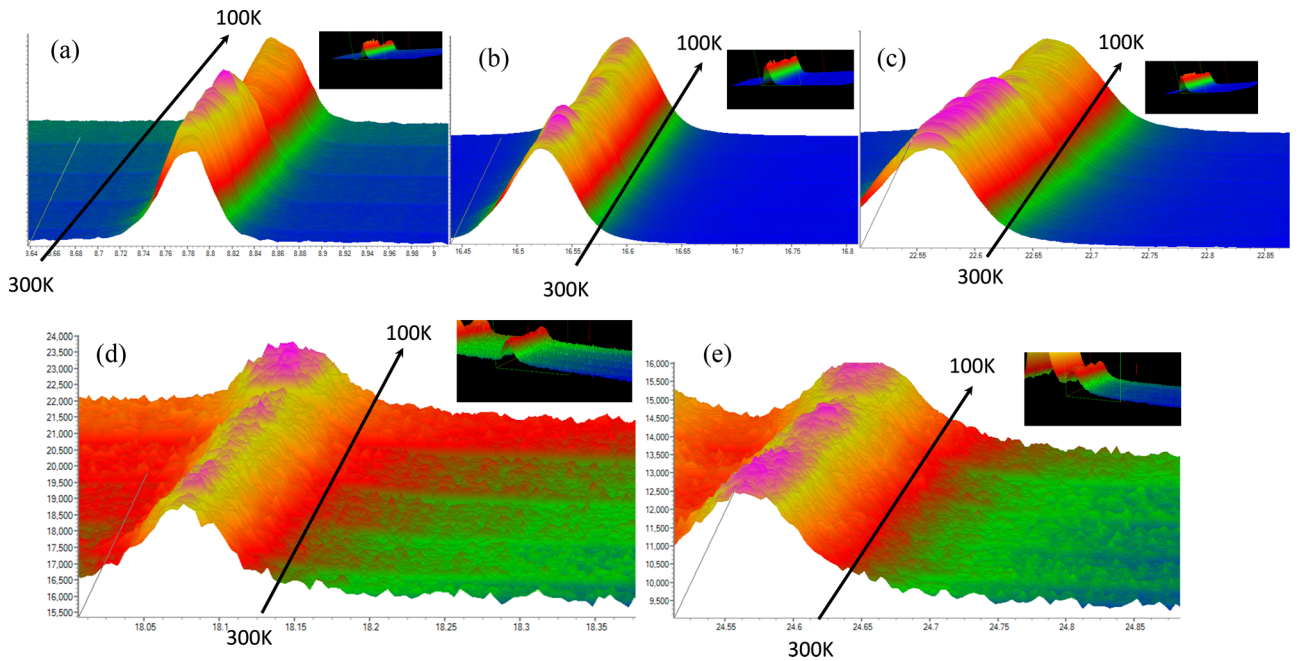

FIG. 2. Thermal evolution of the Bragg reflections of the sample $Rh_{0.75}Ir_{0.25}Te_2$ where y is the intensity (arb. units) and x is 2θ (deg): (a–c) Bragg reflection evolution of the $P\bar{3}m1$ phase (8.7°, 16.5°, and 22.5°) in the temperature range 100—300 K. (d,e) Bragg reflection evolution of the pyrite phase (18° and 24.5°).

TABLE III. Refined unit cell parameters, Te and Ir occupancies (refined compositions), and reliability factors obtained from SR XRPD at 100 K for $IrTe_2$. We quantified the phases: $P\bar{1}$ 93.85% w/w, $P\bar{3}m1$ 4.7% w/w, and elemental Ir 1.45% w/w.

Compound	$IrTe_2$	Reliability factors		Unit cell parameters	
Main phase		R_p (%)	34.2	a Å	6.95604(8)
		R_{wp} (%)	22.2	b Å	6.66230(2)
		R_{exp} (%)	14.99	c Å	14.24540(3)
% w/w	93.85	R_{Bragg} (%)	11.9	V (Å³)	357.760(2)
		R_{factor} (%)	7.26	α (deg)	80.30016
				β (deg)	87.48904
				γ (deg)	72.65700
Atomic positions					
Ir 2 ι (−x, y, z)		Ir 2 ι (x, y, z)		Te 2 ι (x, y, z)	
x	−0.29021(3)	x	0.34957(5)	x	0.35802(4)
y	0.42606(5)	y	0.21978(5)	y	0.15854(5)
z	0.4105(4)	z	0.1996(3)	z	0.38881(6)
Occ	0.97647(5)	Occ	1.01862(2)	Occ	1.10423(5)
Ir 1a (0,0,0)		Te 2 ι (x, y, z)		Te 2 ι (−x, y, z)	
Occ	0.47758(5)	x	0.36218(5)	x	−0.26367(5)
		y	0.28294(5)	y	0.47655(4)
		z	0.02201(5)	z	0.23523(4)
		Occ	1.07793(5)	Occ	0.97300(4)
Te 2 ι (x, y, z)		Te 2 ι (−x, −y, z)			
x	0.07029(4)	x	−0.00637(6)		
y	0.70005(4)	y	−0.03955(6)		
z	0.4077(5)	z	0.19027(6)		
Occ	0.93993(4)	Occ	0.95585(5)		

genides [5]. With increase of the temperature, the magnetic susceptibility is practically temperature independent as is expected for metals. This behavior is typically observed in delocalized conduction electrons (Pauli paramagnetism).

Using the Fermi gas model of noninteracting electrons that predicts that the Pauli magnetic susceptibility is $\chi^0_{Pauli} = \mu_B^2 D(\epsilon_F)$, and using $D(\epsilon_F) = 1.94$ states/eV (obtained from a density of states (DOS) calculation for $IrTe_2$ [37], we obtain
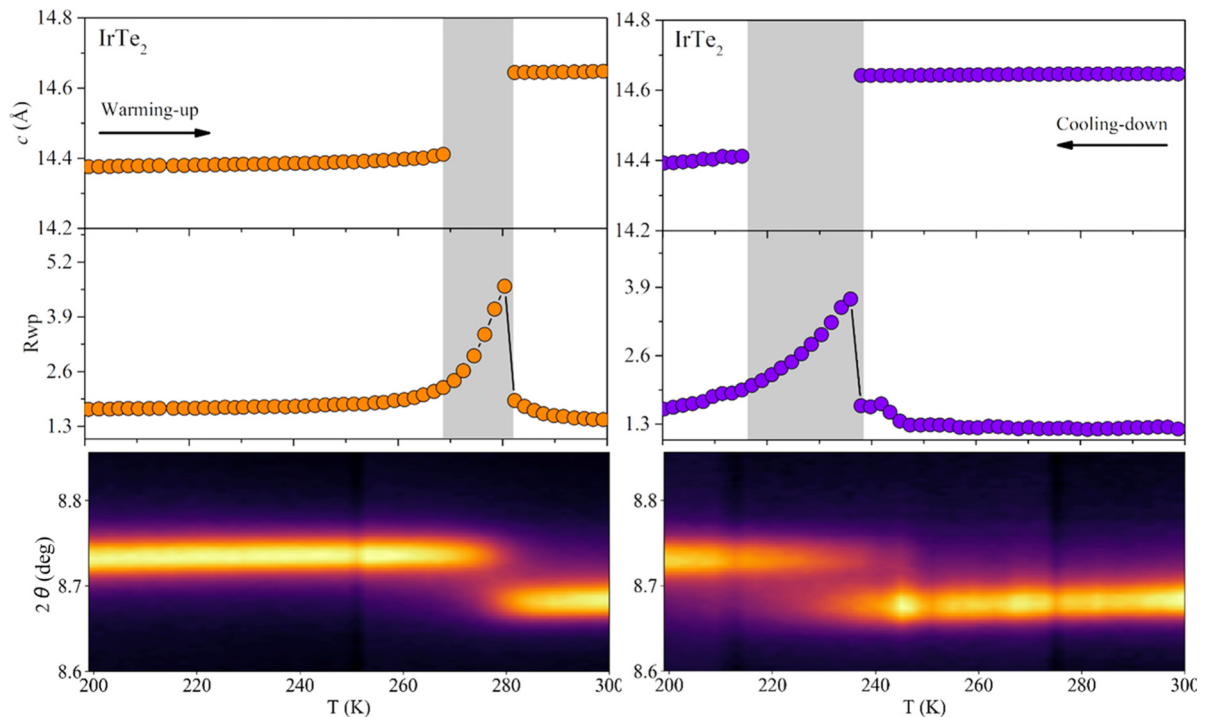

FIG. 3. Temperature-dependent evolution of the c lattice parameter. Also R_{wp} and 2θ (8.6°–8.9°) are plotted. The refinement was performed with a single-phase model ($P\bar{1}$).
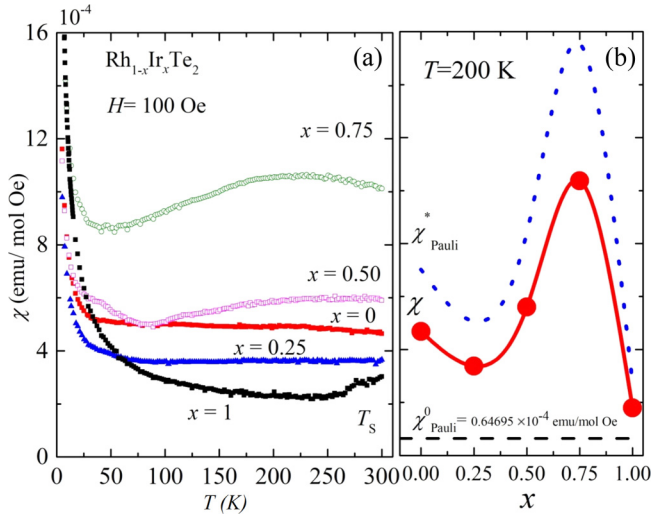
FIG. 4. (a) Magnetic susceptibility in the warming process from 5 to 300 K for $Rh_{1-x}Ir_xTe_2$ ($0 \leqslant x \leqslant 1$). T_S is the observed phase transition temperature. (b) χ at 200 K as a function of x, which is compared with estimated $\chi^0_{Pauli} = 0.64695 \times 10^{-4} \frac{emu}{mol\,Oe}$ for $IrTe_2$ and with χ^*_{Pauli}. These values are obtained subtracting the Landau contribution of the conduction electrons from χ.

FIG. 5. Electrical resistivity as a function of T for $Rh_{1-x}Ir_xTe_2$ ($0 \leqslant x \leqslant 1$) is shown in plots (a,b). We change the ρ scale axis in (b), to show more clearly the samples with a difference between warming and cooling curves. This hysteresis is associated to the first-order structural transition.

$\chi^0_{Pauli} = 0.64695 \times 10^{-4} \frac{emu}{mol\,Oe}$. At 200 K all the compositions show that the experimental values are larger than the Fermi gas model, $\chi_{expt} > \chi^0_{Pauli}$. This indicates that the electrons are interacting with each other, and the Pauli magnetic susceptibility should be corrected by an effective mass factor (m^*/m_e), and consequently $\chi_{expt} = (\frac{m^*}{m_e})\chi^0_{Pauli}$. The magnetic susceptibility of $Rh_{0.75}Ir_{0.25}Te_2$ shows a shoulder in a large temperature range 50–300 K. We can explain this behavior with the temperature dependence of the Pauli paramagnetism $\chi^0_{Pauli}(T)$ that introduces a temperature dependence of high order in the expansion series of the electronic density of states, increasing the magnetization. In the case of $IrTe_2$ a jump is observed at 280 K (T_S), which is associated with the phase transition.

Figure 4(b), as a function of x, shows (i) the magnetic susceptibility (χ) at 200 K represented with a line with filled circles. (ii) The dotted line shows the magnetic susceptibility (χ^*_{Pauli}) obtained as a result of subtracting the Landau susceptibility of the conduction electrons from χ. This value should contain the information about the correlations present in the system. (iii) The expected value for a noninteracting system (χ^0_{Pauli}) is represented by a horizontal dashed line. The ratio $\chi^*_{Pauli}/\chi^0_{Pauli}$ provides an idea of the variation of the effective mass (m^*/m_e) with x, a parameter that describes electron correlations in the system. The Ir-rich compounds present a notable contribution to experimental susceptibility. These high values can be explained by changes in the effective mass parameter instead of changes in the electron density at the Fermi energy, because Ir and Rh do not have significant differences (they are in the same group of the Periodic Table).

C. Electrical and thermal transport properties

The samples are brittle and often cracked; the formation of crack defects is helped by the change of phase during the
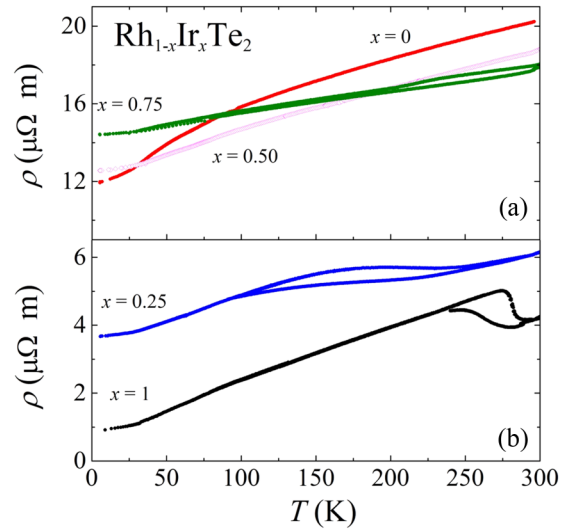
thermal cycling in the resistivity and Seebeck measurements. Sometimes, after the electrical resistivity or Seebeck experiment, we observed cracks, or the sample had broken. In the electrical resistivity experiments, in some cases, we observed that the thermal cycling produces a shift to high values due to the formation of new cracks, which certainly affects the geometrical factor. The resistivity values of Fig. 5 were in all cases in the first thermal running; in the cases where we had doubts, we checked by running with another sample of the same composition.

Figure 5 shows the thermal evolution of electrical resistivity (ρ) for $Rh_{1-x}Ir_xTe_2$. We observe metallic behavior for all the compounds. We observe that the electrical resistivity decreases with temperature for all members of the series, except for $IrTe_2$ around 280 K because it shows a significant thermal hysteresis due to the phase transition observed in the diffraction experiments. $Rh_{0.75}Ir_{0.25}Te_2$ shows a slight thermal hysteresis which suggests a phase transition, in total agreement with the observed changes in the evolution of Bragg reflections of the $P\bar{3}m1$ phase. In future analysis, SR XRPD measurements at lower temperatures ($T < 100$ K) should be performed to elucidate this possible phase transition.

At $T < 50$ K, the temperature dependence of the electrical resistivity [$\rho(T)$] could be described as $\rho(T) \sim T^2$, which can be associated with Fermi liquid behavior. In this temperature range 5–50 K, due to the Fermi liquid behavior, the data were fitted using the expression $\rho(T) = \rho_0 + A_{e-e}T^2$. The A_{e-e} values obtained (see Fig. S4 in the Supplemental Material [31]) are similar for other dichalcogenides with strongly correlated electrons and Sr_2RuO_4 [5,38], which indicate that there is an important electron-electron scattering. The parameter A_{e-e} has the information of the electron density of states at the Fermi level. The residual electrical resistivity (ρ_0) term is sample dependent and lower values indicate high quality

TABLE IV. Parameters A_{e-e}, ρ_0, and $A_{e\text{-ph}}$ for $Rh_{1-x}Ir_xTe_2$ ($0 \leqslant x \leqslant 1$).

Compound	RhTe$_2$	Rh$_{0.75}$Ir$_{0.25}$Te$_2$	Rh$_{0.50}$Ir$_{0.50}$Te$_2$	Rh$_{0.25}$Ir$_{0.75}$Te$_2$	IrTe$_2$
A_{e-e} 10^{-5} ($\mu\Omega\,m/K^2$)	86.9 ± 0.3	17.4 ± 0.1	22.1 ± 0.3	33.5 ± 0.3	18.8 ± 0.5
ρ_0 ($m\Omega\,m$)	13.18 ± 0.01	3.73 ± 0.01	12.69 ± 0.01	14.42 ± 0.01	0.907 ± 0.008
A_{e-ph} 10^{-2} ($\mu\Omega\,m/K$)	1.990 ± 0.004	0.767 ± 0.003	1.880 ± 0.003	1.080 ± 0.003	1.520 ± 0.003

in polycrystalline samples. In Table IV we show A_{e-e} values. Compounds rich in Ir are weaker electron-electron scatterers than those rich in Rh. ρ_0 values are of the same order of magnitude as those estimated for dichalcogenide PdTe$_2$ in a polycrystalline sample and single crystal [5,39,40]. At temperatures higher than 50 K (and depending on the presence and the position of the first-order transition), the data can be fitted with the expression $\rho(T) = \rho_0 + A_{e-ph}T$ where A_{e-ph} is the electron-phonon coupling coefficient, which has typically linear behavior with temperature (see Fig. S5 in the Supplemental Material [31]). The data of the sample IrTe$_2$ were fitted in the temperature range 200–270 K due to the position of the phase transition. In the rest of the compositions the data were fitted in the range 200–290 K. This value is larger compared with Au and Cu, which evidence a strong electron-phonon coupling in these dichalcogenides.

For the samples that present thermal hysteresis in the electrical resistivity, we measured warming and cooling experiments of the magnetic susceptibility at $H = 5$ kOe. We clearly observed the expected thermal hysteresis between 225 and 300 K for $x = 1$, which is associated with the first order and structural transition (T_S). In $x = 0.25$ sample, small differences between the warming and cooling experiments are observable, approximately, between 100 and 250 K (see Fig. S6 in the Supplemental Material [31]).

In the Seebeck experiment, we used copper probes to measure the voltage difference across the input terminals of the nanovoltmeter. This voltage can be expressed as

$$\Delta V = -\left[\int_{T_0}^{T_C} S_{Cu}(T)dT + \int_{T_C}^{T_H} S(T)dT + \int_{T_H}^{T_0} S_{Cu}(T)dT\right],$$

where S is the Seebeck coefficient of the sample; S_{Cu} is the copper Seebeck coefficient used as voltage probes; T_0 is the temperature in the nanovoltmeter terminals; T_H and T_C are the hot and cold temperatures, respectively, at both sample sides of the sample where the voltage probes make contact.

Now, only for the copper probes, we have

$$\int_{T_0}^{T_C} S_{Cu}(T)dT + \int_{T_H}^{T_0} S_{Cu}(T)dT = \int_{T_H}^{T_C} S_{Cu}(T)dT,$$

which simplifies the equation of Δv,

$$\Delta V = -\int_{T_C}^{T_H} [S(T) - S_{Cu}(T)]dT.$$

For small temperature differences ($\Delta T < 1$), the Seebeck coefficient value of the sample and copper probes can be considered as a constant. Assuming $T = T_H + T_C/2$ and $\Delta T \ll$

T we have

$$S(T) = -\frac{\Delta V}{\Delta T} + S_{Cu}(T) = S_{expt}(T) + S_{Cu}(T).$$

In Fig. 6(a) we show the experimental Seebeck coefficient [$S_{expt}(T)$] as a function of temperature, and in Fig. 6(b) we plot the absolute Seebeck coefficient for all compositions in the 80–300 K temperature range, which is obtained adding to $S_{expt}(T)$, the $S_{Cu}(T)$ contribution.

All the $S(T)$ values are positive, indicating the presence of hole-type carriers. IrTe$_2$ shows a hysteresis in $S(T)$ across the structural phase transition temperature (T_S). As the triclinic $P\bar{1}$ phase arises close to T_S, partial localization of hole-type carriers can be responsible of dimer formation [39,41] and changes in the Fermi surface topology are expected. Diffusive Seebeck (S_d) response is reported in the literature [27] for low values of Rh substitution in the IrTe$_2$ compound. This diffusive Seebeck behavior is due to the free electrons that transport heat to equilibrate the gradient of temperature, generating an electric voltage difference in the sample. Seebeck is zero ($S = 0$) at 0 K and S_d increases linearly with temperature, which is observable in the S experiment at $T < 40$ K [27]. As the temperature increases, the phonons contribute with an extra mechanism for conducting heat (phonon drag). This contribution (S_{pd}) to the total Seebeck is practically proportional to the specific heat
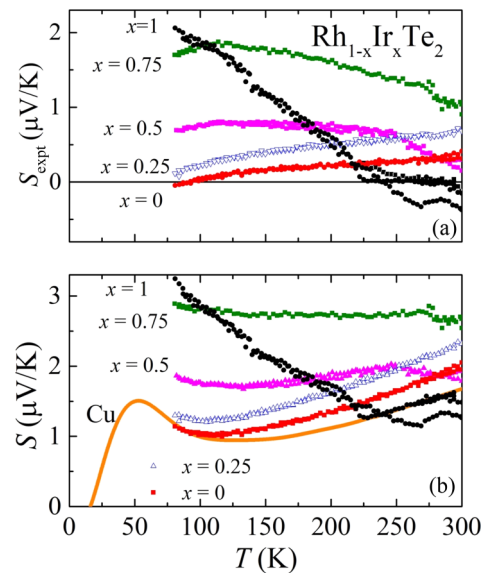

FIG. 6. (a) Experimental Seebeck coefficient for $Rh_{1-x}Ir_xTe_2$ including copper (Cu) probe contributions. (b) Absolute Seebeck coefficient of $Rh_{1-x}Ir_xTe_2$ series. The copper probe contributions have been discounted.

TABLE V. $Rh_{1-x}Ir_xTe_2$, Fermi energies estimated with the Mott formula to describe the Seebeck diffusion of metals [see Eq. (1)] and free electron concentration (n) estimated using the cell volume of Table II and considering $z = 2$.

Compound	Fermi energy (eV)	$n = (z/V)$ (10^{22} electrons/cm^3)
$RhTe_2$	5.6	2.76
$Rh_{0.75}Ir_{0.25}Te_2$	3.5	2.78
$Rh_{0.50}Ir_{0.50}Te_2$	4.4	2.76
$Rh_{0.25}Ir_{0.75}Te_2$	4.8	2.75
$IrTe_2$	6.6	2.76

TABLE VI. Electrical resistivity, Seebeck coefficient, and calculated electronic thermal conductivity at 300 K for $Rh_{1-x}Ir_xTe_2$. Values compared with the two most studied thermoelectric chalcogenides: Bi_2Te_3 and Sb_2Te_3.

Compound	ρ ($\mu\Omega$ m)	S (μV/K)	$\kappa_e = \frac{\mathcal{L}_0 T}{\rho}$ (W/K m)	Carrier/cm^3
$RhTe_2$	20.30	1.99	0.36	$\sim 10^{22}$
$Rh_{0.75}Ir_{0.25}Te_2$	6.11	2.32	1.19	$\sim 10^{22}$
$Rh_{0.50}Ir_{0.50}Te_2$	18.74	1.83	0.39	$\sim 10^{22}$
$Rh_{0.25}Ir_{0.75}Te_2$	17.88	2.66	0.43	$\sim 10^{22}$
$IrTe_2$	4.21	1.47	1.74	$\sim 10^{22}$
Bi_2Te_3	5.5	162	1.468	$\sim 10^{19}$
Sb_2Te_3	1.22	63	5.205	$\sim 10^{19}$

[$S_{pd}(T) \sim C_p(T)$] and its cubic potential temperature growth quickly masks the diffusive contribution. A maximum in S is observable close to $\theta_D/5$, where θ_D is the Debye temperature. The phonon drag is present in a wide range of temperature. Above $T > \theta_D$, C_p is constant and the linear behavior by S_d should be observed again. Also, Ref. [27] reports $\theta_D \approx 200$ K for $IrTe_2$.

The Seebeck coefficient in metals is described by

$$S = \frac{\pi^2 k_B^2 T}{3 e}\left[\frac{\partial \ln \sigma(E)}{\partial E}\right],$$

where k_B is the Boltzmann constant, e is the absolute value of electron charge, and $\sigma(E)$ is the distribution of electrical conductivity in energy (E), which is very complicated to calculate. In general, this equation in the Seebeck diffusive regime of the free electrons is given by the Mott equation:

$$S_d = \frac{\pi^2 k_B^2 T}{2 e \epsilon_F}. \tag{1}$$

ϵ_F is the Fermi energy. We assume that the phonon drag contribution is negligible above $\theta_D \approx 200$ K and the linear behavior observed in S is due to the diffusive contribution. Taking the S values at $T = 250$ K, we estimate ϵ_F using Eq. (1) and the obtained values are shown in Table V. The Fermi energy values are comparable with noble metals (Ag and Au, 5.5 eV). On the other hand, we estimated the electron concentration in the conduction band (Table II), considering that the Ir or Rh atoms contribute with $z = 2$ electrons by unit cell volume (V). These values are comparable with similar dichalcogenides $PdTe_2$ and $Cu_{0.04}PdTe_2$ [5,42].

Unfortunately, it was not possible to measure the thermal conductivity (κ). These measurements require very compact pellets, with $\varphi = \frac{\delta_{expt}}{\delta_{theor}} \sim 99.9\%$, which prevents grain boundary scattering, where $\delta_{expt} = \frac{\text{pellet mass}}{\text{pellet volume}}$ (pellet volume = $\pi h r^2$) and δ_{theor} is determined by Rietveld analysis. Calculations of φ for all the compounds show values of $\sim 60\%$ indicating low density pellets. Results reported in the literature measured with the frequency domain thermoreflectance (FDTR) technique [43] with polished surfaces showed that reflectance was diffuse, and also the signals were extremely low. In addition to the electrical resistivity and Seebeck coefficient, the thermal conductivity is another physical property that is necessary to calculate the figure of merit.

The total thermal conductivity can be understood as the addition of two contributions: $\kappa = \kappa_e + \kappa_L$ where κ_e is the electronic and principal contribution in metals and the second term (κ_L) is the contribution of the lattice. κ_e can be estimated using the Wiedemann-Franz law $\kappa_e = \frac{\mathcal{L}_0 T}{\rho}$, where $\mathcal{L}_0$ is the constant Lorentz contribution $\mathcal{L}_0 = \frac{\pi^2}{3}(\frac{k_B}{e})^2 = 2.45 \times 10^{-8}$ W Ω K^{-2}, and ρ is the experimental electrical resistivity. The estimated κ_e data at room temperature (~ 300 K), which can be the service temperature of a thermoelectric device, are shown in Table VI. In general, κ_L values are estimated subtracting these κ_e values from the total experimental thermal conductivity (κ) or it is assumed as a constant value that depends on the specific heat, mean free path of the phonons, and sound velocity. We also assume that κ_e is larger than κ_L and that $\kappa \approx \kappa_e$ is as it is observed in noble metals (Cu, Ag, and Au) similarly to those reported for $IrTe_2$ and $Ir_{0.9}Rh_{0.1}Te_2$ [27].

In Table VI we show ρ, S, and calculated κ_e values at 300 K for $Rh_{1-x}Ir_xTe_2$. On the other hand, as reference, we compare the electric and thermal transport properties with two of the very well-studied chalcogenides. These compounds are Bi_2Te_3 and Sb_2Te_3, which have good thermoelectric efficiencies [44]. Good thermoelectric values were obtained with carrier concentrations of approximately $n \sim 10^{19}$ carriers/cm^3, which is characteristic of semiconducting materials. The dichalcogenides synthesized in the present work present a strong metallic behavior with $n \sim 10^{22}$ carriers/cm^3. The high n values reduce ρ and κ. On the contrary, the high carrier concentrations are more effective at transporting heat to equilibrate the gradient of temperature, reducing S and notably ZT $\sim S^2$. The figures of merit ZT for our samples of $Rh_{1-x}Ir_xTe_2$, studied in this work, are 10^4 times smaller than Bi_2Te_3 (ZT~ 0.98) or Sb_2Te_3 (ZT~ 0.18) [44]. For future studies, dichalcogenides with heavier elements and semiconducting properties should be synthesized, in order to improve the thermoelectric power.

IV. CONCLUSIONS

We synthesized and characterized the structural, magnetic, electric, and thermoelectric properties of $Rh_{1-x}Ir_xTe_2$ ($0 \leqslant x \leqslant 1$). Quenching from synthesis temperature to liquid nitrogen was essential to obtain the metastable layered phase $P\bar{3}m1$. $RhTe_2$ has been successfully synthesized in the layered $P\bar{3}m1$ phase. $IrTe_2$ shows a first-order phase transition

from the hexagonal to the triclinic phase, which has been monitored with SR XRPD. This is also observed as a thermal hysteresis in the measurements of electrical resistivity, Seebeck effect, and magnetic susceptibility. For $Rh_{0.75}Ir_{0.25}Te_2$, thermal hysteresis and the evolution of Bragg reflections of $P\bar{3}m1$ phase show changes which suggest a structural phase transition. In future analysis, SR XRPD measurements at lower temperatures ($T < 100\,K$) should be performed to elucidate this possible phase transition.

The whole family shows a metallic behavior with an important electron-electron correlation. The expected magnetic Pauli susceptibility is amplified by an effective mass factor. Also, quadratic temperature dependence in the electrical resistivity at low temperature is observed. Both characteristics correspond to a Fermi liquid. On the other hand, the Seebeck experiments allowed the determination of hole-type carriers in all compositions and a dominating electronic diffusion mechanism, which can be described by the Mott formula. The thermoelectric power of these dichalcogenides is lower than the most studied Bi_2Te_3 and Sb_2Te_3 compounds, principally due to the high carrier concentration of our compounds.

[1] D. Greig, Thermoelectricity and thermal conductivity in the lead sulfide group of semiconductors, Phys. Rev. **120**, 358 (1960).

[2] J. Heremans, The ugly duckling, Nature (London) **508**, 327 (2014).

[3] T. Tritt and M. A. Subramanian, Thermoelectric materials, phenomena, and applications: A bird's eye view, MRS Bull. **31**, 188 (2016).

[4] X. Jiang, L Zhu, and K. Yao, Thermoelectric properties of $TcX_2 (X = S, Se, Te)$, J. Alloy Compd. **764**, 505 (2018).

[5] M. K. Hooda and C. Yadav, Electronic transport properties of intermediately coupled superconductors: $PdTe_2$ and $Cu_{0.04}PdTe_2$, EPL **121**, 17001 (2018).

[6] A. Charoenphakdeeab, K. Kurosakia, A. Harnwunggmoungab, H. Mutaa, and S Yamanakaac, Thermoelectric properties of gold telluride: $AuTe_2$, J. Alloy Compd. **496**, 53 (2010).

[7] N. V. Podberezskaya, S. A. Magarill, N. V. Pervukhina, and S. V. Borisov, Crystal chemistry of dichalcogenides MX_2, J. Structural Chemistry **42**, 654 (2001).

[8] J. A. Wilson and A. D. Yoffe, The transition metal dichalcogenides discussion and interpretation of the observed optical, electrical and structural properties, Adv. Phys. **18**, 193 (1969).

[9] S. Kitagawa, H. Kotegawa, H. Tou, H. Ishii, K. Kudo, M. Nohara, and H. Harima, Pressure-induced superconductivity in mineral calaverite $AuTe_2$, J. Phys. Soc. Jpn. **82**, 113704 (2013).

[10] G. Tunell and L. Pauling, The atomic arrangement and bonds of the gold-silver ditellurides, Acta Crystallogr. **5**, 375 (1952).

[11] H. Okamoto and T. Massalski, The Au-Tc (Gold-technetium) system, Bull. Alloy Phase Diagrams **5**, 390 (1984).

[12] S. Jobic, R. Brec, A. Pasturel, H. J. Koo, and M. H. Whangbo, Theoretical study of possible iridium ditelluride phases attainable under high pressure, J. Solid State Chem. **162**, 63 (2001).

[13] Zh. Ding, H. Kleykamp, and F. Thümmler, The constitution of the rhodium-tellurium system, J. Nucl. Mater. **171**, 134 (1990).

[14] V. Abadie, S. Jobic, R. Krachler, H. Ipser, I. Orion, and R. Brec, Single phase domain occurrence in the $Rh_{1+x}Te_2$ ($0.15 \leqslant x \leqslant 0.84$) system, J. Alloys Compd. **268**, 50 (1998).

[15] S. Pyon, K Kudo, and M. Nohara, Superconductivity induced by bond breaking in the triangular lattice of $IrTe_2$, J. Phys. Soc. Jpn. **81**, 053701 (2012).

[16] A. P. Schnyder, S. Ryu, A. Furusaki, and A. W. W. Ludwig, Classification of topological insulators and superconductors in three spatial dimensions, Phys. Rev. B **78**, 195125 (2008).

[17] L. Fu and E. Berg, Odd-Parity Topological Superconductors: Theory and Application to $Cu_xBi_2Si_3$, Phys. Rev. Lett. **105**, 097001 (2010).

[18] D. N. Basov and A. V. Chubukov, Manifesto for a higher T_c, Nat. Phys. **7**, 272 (2011).

[19] G. Saito and Y. Yoshida, Organic Superconductors, Chem. Rec. **11**, 124 (2011).

[20] L. Jiao, Y. Chen, Y. Kohama, D. Graf, E. Bauer, J. Singleton, J. Zhu, Z. Weng, G. Pang, T. Shang, J. Zhang, H. O. Lee, T. Park, M. Jaime, J. D. Thompson, F. Steglich, Q. Si, and H. Q. Yuan, Fermi surface reconstruction and multiple quantum phase transitions in the antiferromagnet $CeRhIn_5$, Proc. Natl. Acad. Sci. USA **112**, 673 (2015).

[21] K. Takubo, K. Yamamoto, Y. Hirata, H. Wadati, T. Mizokawa, R. Sutarto, F. He, K. Ishii, Y. Yamasaki, H. Nakao, Y. Murakami, G. Matsuo, H. Ishii, M. Kobayashi, K. Kudo, and M. Nohara, Commensurate versus incommensurate charge ordering near the superconducting dome in $Ir_{1-x}Pt_xTe_2$ revealed by resonant x-ray scattering, Phys. Rev. B **97**, 205142 (2018).

[22] M. N. Wilson, T. Medina, T. J. Munsie, S. C. Cheung, B. A. Frandsen, L. Liu, J. Yan, D. Mandrus, Y. J. Uemura, and G. M. Luke, μSR and magnetometry study of superconducting 5% Pt-doped $IrTe_2$, Phys. Rev. B **94**, 184504 (2016).

[23] A. I. Galyas and G. Makovestkii, Magnetic phase transitions in the $Mn_{1-x}Cr_xSe$ ($x \leqq 0.4$) system, Cryst. Res. Technol. **20**, 819 (1985).

[24] A. I. Galyas, O. F. Demidenko, G. I. Makovetskiĭ, K. I. Yanushkevich, L. I. Ryabinkina, and O. B. Romanova, Crystal structure and electrical properties of $Gd_xMn_{1-x}S$ and $Ti_xMn_{1-x}Se$ solid solutions, Phys. Solid State **52**, 687 (2009).

[25] J. Guo, Y. Qi, and H. Hosono, Structure and superconductivity in pyrite $Ir_{0.9-x}Rh_xTe_2$: A comparison with analogous selenides, Phys. Rev. B **87**, 224504 (2013).

[26] R Yu, S. Banerjee, H. C. Lei, Ryan Sinclair, M. Abeykoon, H. D. Zhou, C. Petrovic, Z. Guguchia, and E. S. Bozin, Absence of local fluctuating dimers in superconducting $Ir_{1-x}(Pt, Rh)_xTe_2$, Phys. Rev. B **97**, 174515 (2018).

[27] Y. Liu, H. Lei, K. Wang, M. Abeykoon, J. B. Warren, E. Bozin, and C. Petrovic, Thermoelectric studies of $Ir_{1-x}Rh_xTe_2$ ($0 \leqslant x \leqslant 0.3$), Phys. Rev. B **98**, 094519 (2018).

[28] A. Kjekshus, T. Rakke, and A. Andressen, Pyrite-like phases in the Rh-Te system, Acta Chem. Scand. A **32a**, 209 (1978).

[29] H. M. Rietveld, A profile refinement method for nuclear and magnetic structures, J. Appl. Crystallogr. **2**, 65 (1969).

[30] J. Rodriguez-Carvajal, Recent advances in magnetic structure determination by neutron powder diffraction, Phys. B (Amsterdam, Neth.) **192**, 55 (1993).

[31] See Supplemental Material at http://link.aps.org/supplemental/10.1103/PhysRevB.105.104104 for explanatory figures, a table of Rietveld refinement from XRPD SR, SEM images, additional electrical resistivity data and experimental results on magnetic susceptibility.

[32] K. Momma and F. Izumi, VESTA 3 for three-dimensional visualization of crystal, volumetric and morphology data, J. Appl. Crystallogr. **44**, 1272 (2011).

[33] C.-S. Lee and G. J. Miller, Vacancy ordering and bonding competition in the group 9 tellurides M_xTe_2 (M = Rh, Ir; $0.75 \leqslant x \leqslant 2$): A theoretical study, Inorg. Chem. **38**, 5139 (1998).

[34] J. J. Yang, Y. J. Choi, Y. S. Oh, A. Hogan, Y. Horibe, K. Kim, B. I. Min, and S-W. Cheong, Charge-Orbital Density Wave and Superconductivity in the Strong Spin-Orbit Coupled $IrTe_2$:Pd, Phys. Rev. Lett. **108**, 116402 (2012).

[35] K Mizuno, K. Magishi, Y. Shinonome, T. Saito, K. Koyama, N. Matsumoto, and S. Nagata, ^{125}Te NMR study of $IrTe_2$, Physica B: Condensed Matter **312**, 818 (2002).

[36] A. F. Fang, G. Xu, T. Dong, P. Zheng, and N. L. Wang, Structural phase transition in $IrTe_2$: A combined study of optical spectroscopy and band structure calculations, Sci. Rep. **3**, 1153 (2013).

[37] B. Li, G. Huang, J. Sun, and Z. Xing, Novel structural phases and superconductivity of iridium telluride under high pressures, Sci. Rep. **4**, 6433 (2014).

[38] Y. Maeno, H. Hashimoto, K. Yoshida, S. Nishizaki, T. Fujita, J. G. Bednorz, and F. Lichtenberg, Superconductivity in a layered perovskite without copper, Nature (London) **372**, 532 (1994).

[39] Gihun Ryu, Superconductivity in Cu-intercalated CdI_2-Type $PdTe_2$, J. Supercond. Novel Magn. **28**, 3275 (2015).

[40] G. Cao, W. Xie, W. A. Phelan, J. F. DiTusa, and R. Jin, Electrical anisotropy and coexistence of structural transitions and superconductivity in $IrTe_2$, Phys. Rev. B **95**, 035148 (2017).

[41] G. L. Pascut, K. Haule, M. J. Gutmann, S. A. Barnett, A. Bombardi, S. Artyukhin, T. Birol, D. Vanderbilt, J. J. Yang, S.-W. Cheong, and V. Kiryukhin, Dimerization-Induced Cross-Layer Quasi-Two-Dimensionality in Metallic $IrTe_2$, Phys. Rev. Lett. **112**, 086402 (2014).

[42] F. Fei, X. Bo, R. Wang, B. Wu, J. Jiang, D. Fu, M. Gao, H. Zheng, Y. Chen, X. Wang, H. Bu, F. Song, X. Wan, B. Wang, and G. Wang, Nontrivial Berry phase and type-II Dirac transport in the layered material $PdTe_2$, Phys. Rev. B **96**, 041201(R) (2017).

[43] A. J. Schmidt, R. Cheaito, and M. Chiesa, A frequency-domain thermoreflectance method for the characterization of thermal properties, Rev. Sci. Instrum. **80**, 094901 (2009).

[44] H. Scherrer and S. Scherrer, in *CRC Handbook of Thermoelectrics*, edited by D. M. Rowe (CRC Press, Boca Raton, FL, 1995), Sec. D, p. 211.